Influence of Surface Morphology on the Adhesive Strength of Aluminum/Epoxy Interfaces

Sulin Zhang*, Rahul Panat, K. Jimmy Hsia†

Department of Theoretical and Applied Mechanics
University of Illinois, Urbana, IL 61801, USA

Abstract

Adhesively bonded aluminum joints have been increasingly used in automotive industry because of their structural and functional advantages. Interfacial debonding in these joints has become a major concern limiting their performance. The present work is focused on experimental investigation of the influence of surface morphology on the interfacial fracture behavior of aluminum/epoxy interface. The specimens used in this experimental study were made of an aluminum/epoxy bimaterial stripe in the form of a layered double cantilever beam (LDCB). The LDCB specimens were debonded by peeling off the epoxy layer from the aluminum substrate using a steel wedge. Interfacial fracture energy was extracted from the debonding length by using a solution for the specimen geometry based on a model of a beam on an elastic foundation. This model was validated by direct finite element analysis. The experimental observations establish a direct correlation between the surface roughness of aluminum substrate and the fracture resistance of the aluminum/epoxy interface. The results emphasize the importance of choosing surface features at an appropriate length scale in studying their effects on interfacial fracture resistance.

*Current address: Department of Mechanical Engineering, Northwestern University, Evanston, IL 60208, USA.

†Corresponding author. Email: kj-hsia@uiuc.edu, Fax: 1(217) 244 5707.

Keywords: Adhesive bonding; Surface preparation process; Interfacial fracture resistance; Double cantilever beam (DCB); Wedge peeling test.

1 Introduction

Adhesively bonded aluminum joints have been widely used in aerospace and increasingly used in automotive applications because of their low weight-to-strength ratio and improved manufacturability compared to those made by traditional welding techniques. Prior to bonding, aluminum surface is pretreated with certain processes to produce microscale surface morphology. There is strong evidence that this morphology plays a crucial role in the fracture behavior of adhesive bonds [1]. It is thus highly desirable to establish a relationship between adhesive strength of aluminum joints and the aluminum surface morphology by direct experimental measurements. Such relationship would enhance the capabilities in developing new surface pretreatment processes to improve interfacial fracture resistance. Besides engineering applications, such experiments provide a fundamental understanding of the interface adhesion and the interface debonding mechanisms.

Extensive experimental work has been done on the fracture behavior of various interface systems [2–16]. All these experiments have demonstrated that the dominant fracture mechanisms determining the interfacial fracture resistance are strongly affected not only by the properties of the material systems used, but also by the interfacial microstructures. Turner et al. [4] and Turner and Evans [5] evaluated the adhesive strength of different sandwich systems using double cleavage drilled compression (DCDC) specimens. They observed that for a glass–thermoset polymer interface, the crack propagates by finger-like interface decohesions at the crack front. For a sapphire–metal interface, they observed microcavity initiation, growth and coalescence in the metallic adhesive during crack propagation. Such a process has recently been modelled by Zhang et al. [17,18] and Pardoen and Hutchinson [19].

Cazzato and Faber [8] investigated the fracture of an alumina–glass interface by a bend test. They observed that the crack path was not restricted to the interface, and the resulting fracture resistance was almost independent of the alumina surface roughness. Note that in all the above investigations, the fracture energies measured for the interfaces are on the order of tens of J/m^2. Thouless [2] developed an experiment to study a model interface for which frictional effects are minimized. His study revealed the importance of the local phase angle in determining the fracture resistance under mixed-mode loading. Furthermore, it was shown that the fracture path dictates the fracture resistance of adhesive bonds [3]. Thouless [2, 3] concluded that the degree of the surface roughness of the adherend in combination with the mode-mixity determines the interfacial fracture resistance, while the thickness of the adherend has negligible effect on the interfacial fracture resistance.

Particular investigations of metal-epoxy interfaces have also been carried out in the past by Price et al. [9], Brewis and Critchlow [10], Kalnins et al. [11], Zhang and Spinks [12], Mannelqvist and Groth [15], and Sancaktar and Gomatam [16]. Price and Sargent [9] used specimens comprised of a thin toughened epoxy adhesive layer on an aluminum substrate to study the influence of the epoxy thickness on the adhesion strength. They found that increasing the epoxy thickness enhances the peeling strength of the specimens. The authors, however, did not calibrate the peeling strength of their specimens in terms of interfacial fracture mechanics parameters, such as phase angle of loading and the interfacial fracture energy. Brewis and Critchlow [10] investigated the adhesive strength of T-peel joints made of various adhesives and aluminum substrates. The aluminum surfaces were prepared by various electrochemical pretreatments. They established a direct relationship between the surface pretreatments and the peeling force of delamination for the specimens. In this study, however, the surface morphologies related to the surface pretreatments remained to be characterized. Several distinct failure modes were observed in their study, including interfacial failure, and cohesive failure within the adhesive and the

oxide. Kalnins et al. [11] studied the effects of surface roughness on the peeling strength of a steel/epoxy/steel sandwich specimen. They argued that the real contact area between the epoxy and the steel substrate was different from the actual steel surface area. This real contact area was believed to be the parameter that would determine the adhesion strength. Due to the experimental difficulties in measuring the real contact area, they characterized the surface roughness using idealized geometries to approximate the actual surface features observed under a scanning electron microscope (SEM). They found that the peeling strength of the sandwich specimen increases with the surface roughness parameter they used. Similar to Brewis and Critchlow [10], these authors did not use interfacial fracture parameters in their analysis. Furthermore, the use of their surface roughness parameter is not expected to reveal all the possible mechanisms active during delamination.

Zhang and Spinks [12] investigated the effect of surface roughness on the fracture energy of an aluminum–epoxy interface using a lap shear test on a width-tapered cantilever beam. The aluminum surface used in their study was processed by the forest products laboratory etching procedure (FPL). They found that the interfacial fracture energy lies within the range of 29 to 263 J/m^2, and nearly linearly proportional to the fraction of the aluminum area etched by the FPL procedure. They attributed the increase of interfacial fracture resistance exclusively to the increase of the area of the aluminum substrates due to the etching process. Mannelqvist and Groth [15] studied the adhesive strength of an epoxy–steel interface using a tensile lap-shear test. They used fractal analysis to characterize roughness of the steel surface. They found that the tensile strength generally increases with the fractal dimension. Sancaktar and Gomatam [16] measured the strength of a single lap joint made of steel, Epon 815, and Epon 830. The steel surface was pretreated by an etching procedure that results in microroughness on the surface. In their experiments, they revealed that the strength of the joint is generally enhanced as the surface roughness increases. In spite of these studies, the underlying fracture mechanisms related to the surface roughness

that cause the delamination of the layered specimens remain to be investigated.

A primary challenge in the measurement of interfacial fracture resistance is the design of test specimen configurations that provide controlled, stable growth of interfacial cracks. A number of specimen configurations have been suggested in the past decade, including double cantilever beam (DCB) [20], four-point flexural specimen [21], and DCDC specimen [4]. The DCDC configuration has been exploited in the measurement of metal/ceramic interfaces [4, 5] and fracture in homogenous materials [22, 23]. The precrack required in such systems is commonly obtained by cyclic loading of the specimens. The aluminum/epoxy interface is, however, insensitive to cyclic loading, making it difficult to introduce the required high-quality interfacial precrack. A fatigue precrack in such systems inevitably undergoes crack-tip blunting. Propagation of a blunted crack requires both stress and energy criteria to be satisfied [24]. This stress is normally high, causing an unstable crack propagation.

The DCB configuration is frequently chosen because of the simplicity of its geometry and the resulting ease of calibration. Furthermore, a high-quality interfacial precrack can be easily introduced in such a configuration. In the present study, a two layered double cantilever beam (LDCB) specimen is chosen instead of the commonly used three-layer DCB sandwich cantilever beam. A wedge peeling load is applied to propagate the interfacial crack. This bilayer specimen not only ensures stable crack propagation, but also facilitates monitoring of the debond front.

In the present work, a systematic study is undertaken to investigate the effects of various aluminum surface morphologies on the fracture resistance of the aluminum–epoxy interface. A series of surface morphologies are produced for this purpose and characterized by SEM micrographs and line scans using a profilometer. A wedge peeling test on the LDCB specimens is used to investigate the interfacial debonding behavior. The interfacial fracture energy is extracted from the test using a closed-form solution of a "beam on an elastic foundation" model [25]. A finite-element analysis is used to validate this model. Possible interfacial fracture mechanisms affecting the

adhesion strength are discussed.

2 Experimental Procedure

2.1 Material System

The bilayer material system chosen for this study consists of an Al alloy (6061) and an epoxy adhesive (type DP270, 3M Corporation, St. Paul, MN). The composition of the alloy is given elsewhere [26]. The properties of the epoxy can be obtained from the 3M website[1]. The Young's modulus of the epoxy was determined by a compression test of a cylindrical bar, 18.8 mm in diameter and 25 mm in length, on a universal testing machine (UTM) (Instron Corp, Canton, MA). Before the compression test, the epoxy was heated to 160°C with a hold time of about two hours, then furnace-cooled and placed at room temperature for two days. This process fully cures the epoxy. The fully-cured epoxy is off-white, facilitating visualization of the crack front in the fracture experiment. The stress–strain curve measured by the UTM is shown in Fig. 1. The Young's modulus of the epoxy is taken as the slope of the linear part of the curve since this value of 1.13 GPa is only a fraction of the stiffness of the loading mechanism of the UTM. The Poisson's ratio for the epoxy is about 0.4 [27].

2.2 Specimen Preparation

Different surface morphologies of the aluminum alloy were produced and categorized into two groups based on the surface preparation processes used. The first and second groups were made from aluminum plates of thickness 4 mm and 2 mm, respectively. One side of each of the plates was finely polished down to 1 micron using diamond paste. As a baseline surface condition, the surface morphology of the polished aluminum surface and its line scan are shown in Fig. 2. The amplitude of surface rough-

[1] http://www.3m.com

ness is on the order of 75 nm. These plates were sliced into rectangular pieces, 55 mm long and 5 mm wide. The polished surfaces of the first group were repolished using different grit SiC grinding papers (Buehler Ltd., Lake Bluff, IL) (No. 60, 180, 320, and 600). The polishing direction was perpendicular to the crack propagation direction of the specimens. For comparison, aluminum specimens without any repolishing were also included in the first group. A representative surface morphology is shown in Fig. 3. For the second group, the polished aluminum surface was oxidized using a coaxial rotating, axially translating electrochemical reactor (CRATER) developed by Gao et al. [28, 29]. This oxidation process was used to produce three types of surface morphologies, each with uniformly distributed pores of approximately 15, 25, and 40 nm in size, corresponding to an applied voltage of 2.8V, 5.8V and 9.6V, respectively. A representative surface morphology from the second group is shown in Fig. 4. Other than the difference in surface treatment methods, the only difference of the specimens in the first and the second groups is their thicknesses. In addition, a one-side fine-polished sapphire sample (Coating & Crystal Technology Inc., Kittanning, PA) with dimensions identical to the aluminum specimens in the second group was used in this study to provide a baseline value of fracture resistance.

For clarity, the specimens mentioned above are categorized in terms of the surface treatments used. An identification number is assigned to each type of specimen, as listed in Table 1. Sample identifications starting with 'G' and 'D' fall in the first group, while those starting with 'O' fall in the second. Table 1 gives the surface treatment method applied and the roughness index for each type of the samples. The roughness index, R, of the surface is defined as [11, 16, 30]

$$R = \frac{\Delta A}{A_0}, \tag{1}$$

where the area increment, $\Delta A = A - A_0$, with A being the real surface area of the aluminum surface and A_0 being the corresponding projected surface area.

The aluminum slices were coated with a 2 mm thick epoxy layer to form LDCB specimens. The epoxy in these specimens was fully cured by a process identical to

that used for the epoxy cylindrical bar. Extra epoxy on the specimens was carefully polished off. Furthermore, the side surfaces of the specimens were polished by 600-grit SiC paper to enhance crack-tip visualization.

2.3 Surface Characterization

Morphology of the pretreated aluminum surfaces was characterized by line scans in the crack propagation direction using a profilometer (Dektak, Sloan Technology, Santa Barbara, CA) at the Frederick Seitz Materials Research Laboratory (FSMRL), University of Illinois (UIUC). Several scans, each with a full scale of 1000 μm were taken for each type of the aluminum surfaces. This scan scale is thought to be long enough to capture the characteristic surface fluctuations of interest. The actual distance along the scan line is calculated by numerical integration of the data points. The roughness index is then approximated by the ratio, $\Delta l/l_0$, where Δl is the length increment of the actual surface, while l_0 is the corresponding projected scan line length. Line scans of representative surfaces are shown in Figs. 2, 3 and 4. The roughness index value for each of the surfaces listed in Table 1 represents the statistical average of that obtained from at least four line scans. Atomic force microscopy (AFM) was also used to characterize the surface of the specimen O9-4 at different resolutions, as discussed in § 6.

2.4 Testing Apparatus and Procedure

Figure 5 shows a picture of the testing apparatus (Fig. 5(a)) along with a schematic (Fig. 5(b)). The apparatus consists of two micrometers, a stationary base, and three translation stages, denoted by M-1, M-2, SB, TS-1, TS-2 and TS-3, respectively. M-1 and M-2 that control TS-1 and TS-2 are not shown in Fig. 5(b). The translation stage TS-1 is mounted onto SB, and is movable in the x-direction (0–40 mm range). It serves as a master stage on which TS-2 and TS-3 are mounted. The translation stage TS-2 is also movable in the x-direction (0–25 mm range). The positions of TS-1

and TS-2 can be determined from the micrometers, M-1 and M-2, with an accuracy of 0.01 mm.

A wedge made of high speed tool steel (T-series) is attached to a fixture, which is mounted onto TS-2. The wedge is 15 mm long, 0.8 mm thick and has a width W approximately equal to that of the specimens. Specimens are held by a fixture that is mounted on TS-3 with the interface of interest being in the xy plane. The translation stage TS-3 is movable in the z direction with a 6 mm translation capacity. By adjusting TS-3, the aluminum–epoxy interface is aligned with the wedge.

A Nikon optical microscope is positioned above the testing apparatus to monitor the moving crack tip. Aided by a mini-light placed at the bottom of the specimen, a video camera at the side of the specimen records the crack front through the off-white epoxy thickness.

Before mounting a specimen onto the fixture, it is precracked on one end by a sharp blade. The length of the precrack, a_0, is recorded using the microscope. Then, TS-1 and TS-2 are both adjusted to their extreme positions while placing the crack tip in the view of the microscope. Pushing the wedge by moving TS-2 propagates the interfacial crack. By adjusting TS-1, the crack tip remains within the view of the microscope. The effective crack length, a, defined as the distance from the crack tip and the wedge tip, can be determined by

$$a = a_0 + [s - s_0] - [q - q_0], \tag{2}$$

where s_0 and q_0 are the initial positions of TS-1 and TS-2, corresponding to a_0, while s and q are the positions of TS-1 and TS-2, corresponding to a.

3 Specimen Calibration

Interfacial fracture resistance, $\mathcal{G}_c$, can be evaluated by measuring the critical energy release rate at the onset of stable crack growth. For the specimen schematically shown in Fig. 6, the energy release rate, $\mathcal{G}$, can be expressed as a function of the geometry

of the specimen and the material constants, as

$$\frac{\mathcal{G}}{E_{\rm ep}h_{\rm ep}} = F\left(\frac{a}{h_{\rm ep}}, \frac{c}{h_{\rm ep}}, \frac{\delta_y}{h_{\rm ep}}, \frac{h_{\rm Al}}{h_{\rm ep}}, \frac{E_{\rm ep}}{E_{\rm Al}}\right), \tag{3}$$

where $h_{\rm ep}$, $h_{\rm Al}$ and δ_y are the thicknesses of the epoxy, the aluminum substrate and the wedge, respectively, c is the length of the unbounded portion of the epoxy, l is the total length of debonded portion, while $E_{\rm ep}$ and $E_{\rm Al}$ are the Young's moduli of the epoxy and aluminum, respectively.

The dimensionless function in Eq. (3) can be approximately evaluated by three different methods, as described below.

3.1 Simple Beam Theory

Since aluminum substrate ($E_{\rm Al}$ = 69 GPa) is much stiffer than epoxy ($E_{\rm ep}$ = 1.13 GPa), elastic strain energy stored in the aluminum substrate may be neglected as a first approximation. The debonded portion of the epoxy can be modeled as a cantilever beam. The reaction force, F_y, corresponding to the applied displacement, δ_y, at the contacting point between the wedge and the epoxy can be written as

$$F_y = \frac{E_{\rm ep}\delta_y b}{4}\left(\frac{h_{\rm ep}}{a}\right)^3. \tag{4}$$

where b is the dimension of the epoxy (or aluminum) beam in z-direction in Fig. 6. By definition, the compliance of the beam is

$$C_0 = \frac{\delta_y}{F_y} = \frac{4a^3}{E_{\rm ep}bh_{\rm ep}^3}. \tag{5}$$

The energy stored in the epoxy beam, Λ, is

$$\Lambda = \frac{1}{2}\frac{\delta_y^2}{C_0} = \frac{E_{\rm ep}b}{8}\left(\frac{h_{\rm ep}}{a}\right)^3\delta_y^2. \tag{6}$$

The energy release rate $\mathcal{G}$ is given by,

$$\mathcal{G} = -\frac{1}{b}\frac{\partial\Lambda}{\partial a} = \frac{3}{8}E_{\rm ep}\left(\frac{h_{\rm ep}}{a}\right)^3\frac{\delta_y^2}{a}. \tag{7}$$

3.2 Beam on an Elastic Foundation

To estimate the energy release rate using the simple beam theory is a good approximation when the effective crack length, a, is at least five times the thickness of the epoxy beam. Moreover, modeling the unbounded portion of the beam as a clamped end overestimates the stiffness of the structure, leading to an overestimation of the energy release rate. For a more accurate estimate, the energy stored in the bonded portion needs to be taken into account.

Kanninen [25] proposed an approach for determining the energy release rate of such a LDCB specimen. This approach models the specimen as a beam partially free and partially supported by an elastic foundation with stiffness k (see Fig. 7). To establish the relationship between the applied load and the displacement at the loading point, one can invoke the governing equations for the beam deflection $w(x)$,

$$\frac{d^4w}{dx^4} + 4\lambda^4 H(x)w = 0, \tag{8}$$

where $H(x)$ is a step function defined as

$$H(x) = \begin{cases} 1 & , \quad x > 0 \\ 0 & , \quad x \leq 0 \end{cases}$$

and

$$\lambda = \left(\frac{k}{4E_{\text{ep}}I_{\text{ep}}} \right)^{1/4},$$

where I_{ep} is the bending moment of inertia of the epoxy beam.

The appropriate boundary conditions are a shear force P at the loading point (the wedge tip) and a homogeneous boundary condition at $x = c$, as

$$w''(-a) = 0, \tag{9}$$

$$w'''(-a) = P/E_{\text{ep}}I_{\text{ep}}, \tag{10}$$

$$w''(c) = w'''(c) = 0. \tag{11}$$

where c is the portion of the beam supported by the elastic foundation, Fig. 7.

Details of the solution of the above equations are given in Kanninen [25] and Dai et al. [31]. The solution establishes a relationship between the applied load and the displacement at the loading point. The compliance of the structure can be obtained as

$$C_p = \frac{w(-a)}{P} = C_0\Phi, \tag{12}$$

where

$$\Phi = 1.0 + k_1\frac{h_{\rm ep}}{a} + k_2\frac{h_{\rm ep}^2}{a^2} + k_3\frac{h_{\rm ep}^3}{a^3} \tag{13}$$

and

$$k_1 = \frac{3}{\lambda h_{\rm ep}}\left(\frac{\sinh\lambda c\,\cosh\lambda c + \sin\lambda c\,\cos\lambda c}{\sinh^2\lambda c - \sin^2\lambda c}\right), \tag{14}$$

$$k_2 = \frac{3}{\lambda^2 h_{\rm ep}^2}\left(\frac{\sinh\lambda c\,\cosh\lambda c - \sin\lambda c\,\cos\lambda c}{\sinh^3\lambda c - \sin^3\lambda c}\right), \tag{15}$$

$$k_3 = \frac{3}{2\lambda^3 h_{\rm ep}^3}\left(\frac{\sinh\lambda c\,\cosh\lambda c - \sin\lambda c\,\cos\lambda c}{\sinh^2\lambda c - \sin^2\lambda c}\right). \tag{16}$$

The foundation stiffness, k, can be estimated by assuming the aluminum substrate as a series of springs. The deflection that defines the transverse displacement of the central line of the epoxy beam is due to the stretch of the elastic foundation,

$$\sigma(x) = \frac{kw(x)}{b} = \frac{E_{\rm Al}w(x)}{h_{\rm Al}} \tag{17}$$

where $\sigma(x)$ is the load on the aluminum substrate per unit length in x-direction (Figs. 6 and 7). From Eq. (17), one has

$$k = \frac{E_{\rm Al}b}{h_{\rm Al}} \tag{18}$$

and

$$\lambda = h_{\rm ep}\left(\frac{3E_{\rm Al}h_{\rm ep}}{E_{\rm ep}h_{\rm Al}}\right)^{1/4}. \tag{19}$$

The strain energy can be written as

$$\Lambda = \frac{1}{2}\frac{\delta_y^2}{C_p} \tag{20}$$

and the energy release rate is

$$\mathcal{G} = \frac{1}{2b}\frac{\delta_y^2}{C_p^2}\left[\Phi\frac{\partial C_0}{\partial a} + C_0\frac{\partial \Phi}{\partial a}\right] = \frac{3C_0}{2ab}\frac{\delta_y^2}{C_p^2}\left[1 + \frac{2}{3}k_1\frac{h_{\text{ep}}}{a} + \frac{1}{3}k_2\frac{h_{\text{ep}}^2}{a^2}.\right] \tag{21}$$

Note that the energy release rate is independent of the parameter k_3. The energy release rate predicted by this model can always be reduced to that obtained by the simple beam theory by assuming the elastic foundation to be infinitely stiff, i.e., by letting $\lambda \to \infty$, with vanishing k_1, k_2, and k_3.

Our calculation for different values of c shows that the energy release rate is nearly independent of c provided that $c \geq 2h_{\text{ep}} = 4$ mm. For simplicity, all calculations are based on the condition of $c \gg h_{\text{ep}}$. For the specimen configurations, our calculations give

$$k_1 = 0.974, \quad k_2 = 0.316, \quad k_3 = 0.051 \tag{22}$$

for the specimens in the first group, and

$$k_1 = 0.819, \quad k_2 = 0.224, \quad k_3 = 0.031 \tag{23}$$

for the specimens in the second group.

3.3 Finite-element Analysis

A finite-element model was constructed using ANSYS (version 5.7) to analyze the specimens and verify the theoretical models. Plane-strain condition was applied in this analysis. At the tail of the crack, a displacement $\delta_y = 0.8$ mm in the y direction was prescribed at the bottom side of the epoxy beam. The effective crack length was taken in the range of 5 mm to 20 mm. Six-node, triangular elements were used for the epoxy beam and aluminum substrate. Two approaches were used to calculate the energy release rate, as presented below.

3.3.1 Stress Method

The stress method calculates the stress field accurately in the vicinity of the crack-tip by refining the mesh in that region. To ensure accurate estimation of the energy

release rate, the element size around the crack tip must be at least 10^{-3} times the typical dimension of the specimen (e.g., the thickness $h_{\rm ep}$). Furthermore, to estimate the stress intensity factors $K_{\rm I}$ and $K_{\rm II}$ accurately, the stress values for the first 7 to 10 elements from the crack tip should not be used. In our analysis, stresses of the 10th and subsequent elements ahead of the crack-tip were used to calculate the stress intensity factors. The boundary conditions are such that the displacements of the ends of aluminum substrate are zero. The energy release rate is then calculated using the stress intensity factors [32]. Our result shows that, at a given effective crack length a, the energy release rate is nearly independent of the total debonding length, l.

Mode mixity is an important parameter for interfacial cracks [32]. According to our numerical analysis, the mode-mixity of LDCB specimen is nearly independent of the thickness of the aluminum substrate, and weakly dependent on the effective crack length. For the effective crack length ranging from 8 mm to 20 mm, the mode-mixity falls in the range of $-42^\circ \pm 2^\circ$.

3.3.2 Energy Method

The energy method estimates the elastic strain energy stored in two similar configurations. These two geometries, denoted by I and II, differ only in the effective crack length, denoted by $a_{\rm I}$ and $a_{\rm II}$, respectively ($a_{\rm II} - a_{\rm I} = \Delta a$). The boundary conditions are the same as those used in the stress method. Analyzing each configuration with the same mesh density, one can obtain the values of total strain energy of the epoxy beam/aluminum substrate system. By definition, the energy release rate can be estimated by

$$\mathcal{G} = -\frac{\Lambda_{\rm II} - \Lambda_{\rm I}}{\Delta a}, \tag{24}$$

where $\Lambda_{\rm I}$ and $\Lambda_{\rm II}$ are the strain energies stored in the configuration I and II, respectively. In the calculation, the energy release rate converges quickly as Δa decreases. When Δa is in the range of 1% to 0.5% of $a_{\rm I}$, the variation of the energy release rate

is negligibly small. In our calculations, Δa is consistently taken to be 0.5% of a_{I}.

An advantage of this approach is that it does not require ultra fine mesh at the crack tip, thus significantly reducing the computational complexity. However, the calculated stress at the crack tip is not accurate due to the coarse mesh used, and hence cannot be used estimate the mode-mixity. Our numerical results demonstrate that the values of the energy release rate calculated by the stress and energy methods are within 1.5% of each other, validating both methods.

3.4 Comparison

The results obtained from these three calibration approaches are presented in Fig. 8. It shows that when the effective crack length is greater than 12 mm, all three methods give approximately the same energy release rate data. For an effective crack length less than 9 mm, the simple beam theory predicts higher energy release rate than the other two methods. However, the "beam on an elastic foundation" model predicts an energy release rate of less than 5% in difference from that obtained by finite-element analysis, provided that the effective crack length is greater than 6 mm.

4 Effect of Friction

A major concern on the wedge peeling test is the friction between the wedge and the specimen. Such a friction provides an extra driving mechanism for the interfacial crack propagation. To validate the calibration of the specimen, one needs to estimate the effect of friction. The frictional force, F_f, can be estimated from the reaction force, F_y, at the wedge end, as

$$F_f = \mu F_y, \tag{25}$$

where μ is the friction coefficient between the wedge and the epoxy. A simple test of sliding the epoxy on an inclined steel surface gives $\mu \approx 0.3$. The displacement in the

horizontal direction, δ_x, due to the friction force can be calculated by

$$\delta_x = \frac{F_f a}{E_{\rm ep} b h_{\rm ep}} + \frac{F_f h_{\rm ep}^2 a}{4 E_{\rm ep} I_{\rm ep}} = \frac{4 F_f a}{E_{\rm ep} b h_{\rm ep}}, \tag{26}$$

The first term in Eq. (26) results from the axial deformation, while the second term comes from bending. Substituting Eqs. (4) and (25) into Eq. (26), one has

$$\delta_x = \mu \left(\frac{h_{\rm ep}}{a} \right)^2 \delta_y. \tag{27}$$

The energy stored in the epoxy beam due to the frictional force is

$$\Lambda_f = \frac{1}{2} F_f \delta_x = \frac{\mu^2 E_{\rm ep} b}{8} \left(\frac{h_{\rm ep}}{a} \right)^5 \delta_y^2. \tag{28}$$

From Eq. (6) one has

$$\frac{\Lambda_f}{\Lambda} = \mu^2 \left(\frac{h_{\rm ep}}{a} \right)^2. \tag{29}$$

Equation (29) shows that the energy stored in the epoxy beam due to friction is negligibly small compared to bending energy stored in the epoxy beam, even for high friction coefficients. Thus, the friction effect is ignored in the calculation of the energy release rate.

5 Results

Due to stress relaxation in the epoxy, the effective crack length measured in the experiment is dependent on loading rate, i.e., wedge velocity. Experiments using DP-5 specimens show that, for loading rates higher than about 1.2 mm/s, the effective crack length remains almost unchanged (variation with higher loading rate less than 5%). To avoid loading-rate dependence, all the experiments are carried out in the present work using a loading rate higher than about 1.5 mm/s. All the tests are run at room temperature (about 70°F) in ambient air.

Optical observations during the testing revealed that initial debonding occurs in the form of small patches ahead of the crack tip upon pushing the wedge, as seen in

Fig. 9 for a G60 specimen. These patches coalesce upon pushing the wedge further, and eventually connect to the main crack. New debonded patches would then start to form ahead of the new crack front. The crack, therefore, propagates in a jerky manner, jumping intermittently as it grows. The jerkiness during crack propagation is influenced by the surface morphologies of the aluminum substrate, consistent with the experimental observations by Turner and Evans [5]. In general, rougher surfaces give rise to bigger jumps, whereas smoother surfaces result in smaller jumps for a given wedge speed. It is expected that some plastic flow must be present at the crack front preceding each crack jump. Examinations of fracture surfaces by optical microscope revealed no epoxy on the smoother aluminum surfaces, while rare isolated epoxy patches could be seen on the rougher surfaces.

A representative debonding front highlighted by a black dye penetrant as observed using the video camera is shown in Fig. 10. The crack front exhibits a typical arc-like shape, indicating a plane-stress condition on the side surface of the specimen, and a plane-strain condition near the center. When measuring the crack length using an optical microscope, this arc shaped crack front leads to an underestimation of about 0.4 mm to 0.65 mm in the effective crack length. In compiling data in the present experiments, 0.5 mm is added to the measured effective crack length. The difference of 0.1 mm in the effective crack length leads to an insignificant difference in the evaluation of fracture energy (less than 1%).

Based on the corrected effective crack length, the interfacial fracture resistance is estimated by the "beam on an elastic foundation" model. Figure 11 shows the variation of the fracture resistance in terms of the total debonding length for representative specimens (G180 and DP-5). It is evident that the energy release rate is essentially independent of crack extension. This is generally true for all the other specimens with different surface pretreatments.

Figure 12 shows the dependence of the interfacial fracture resistance on the surface roughness. Each data point in this figure represents the measurements for three spec-

imens that had the same surface treatment. Among all the specimens, the specimen with sapphire substrate has the lowest interfacial fracture resistance, which serves as a baseline of fracture energy for the other specimens. The fracture resistance of specimens with different oxidized surfaces exhibits little variation, and is comparable with specimen DP-5, the one with 1 μm diamond paste polished surface. The scattering of the measurements increases with increasing surface roughness. Figure 12 reveals a clear trend that the interfacial fracture resistance is enhanced as surface roughness increases. Note, however, that this relationship is nonlinear.

6 Discussion

The experimental technique developed in the present study has several advantages. The wedge peel test using the LDCB specimen provides controlled, stable interfacial crack propagation. From the calibration curve of the energy release rate for this specimen, it is evident that this specimen is very stable. Use of the off-white epoxy allows us to monitor the crack front using a video camera; such monitoring would not be possible for three-layered sandwich specimens. Furthermore, the uniform thickness of the wedge simplifies the calibration of the energy release rate of the specimen. The present authors also tried to use DCDC specimens [6] to measure the interfacial fracture resistance. However, we found DCDC specimen rather unstable even with attempts to introduce sharp initial crack by cyclic fatigue.

It should be noted that the interfacial fracture resistance measured in the present experiment is approximately in the same range as that measured by Zhang and Spinks [12], and is somewhat higher than those measured by others [7, 13, 31]. The surface roughness may account for these higher values [12]. The surface roughness gives rise to larger contacting surface area between the aluminum substrate and epoxy, thus requiring higher surface energy during the peeling process. However, surface energy alone cannot explain the fracture resistance increase. The nonlinear dependence of

interfacial fracture resistance on surface roughness (see Fig. 12) indicates that other mechanisms may be active during the fracture process.

Under optical microscope, bridging was observed behind the extending interfacial crack for specimens in both groups. Figure 9 shows bridging in a G60 specimen over a distance of about 250 μm from the crack-tip. The bridging ligaments behind the crack tip would enhance fracture resistance significantly. A bridging law is necessary to evaluate the bridging effect. The waviness of the aluminum surface also suggests the existence of local mixed mode loading at the crack-tip, even under far field Mode I loading. This will also enhance the interfacial fracture resistance.

It is important to note that, when seeking to identify the relationship between surface morphology and interfacial fracture resistance, features on the appropriate length scale should be considered. For the surfaces considered in the present study, the values of surface roughness index, R, used to characterize the aluminum surfaces may be dependent on the details of measurements. The reason for this is that the surface features may be fractal in nature [33]. Figure 13 shows three AFM scans of the CRATER treated surface of specimen O9-4 with different resolutions. Figures 13 (a), (b), and (c) are scans of the same spot on the specimen with full scanned lengths of 140 μm, 14 μm, and 350 nm, respectively, corresponding to a lateral resolution of about 400 nm, 40 nm, and 1 nm, respectively. It is evident that the roughness features of the surface are self-similar at length scales spanning more than two orders of magnitude, characteristic of a fractal geometry. As a result, the roughness index evaluated by Eq. (1) has a higher value when using measurements with a higher resolution. In the current study, we used the measurements from profilometer scans to correlate the fracture resistance data in Fig. 12. These measurements have a lateral resolution of about 250 nm, and highlight the roughness features in microscale rather than in nanoscale. As shown in Fig. 9, the dominant processes controlling interfacial fracture, e.g., the bridging and the coalescence of microcracks with the main crack, occur at a length scale of tens of microns. Therefore we believe that the

profilometer measurements possess the resolutions to characterize the appropriate length scale. An indirect evidence of this belief, shown in Table 1 and in Fig. 12, is that the three CRATER treated surfaces have nearly the same values of roughness index when measured by profilometer, although their nanoscale features such as the nanoscopic pore sizes are rather different. The interfacial fracture resistance values of these three surfaces are, not surprisingly, essentially equal.

7 Conclusions

In the present work, effects of surface morphology on the fracture resistance of aluminum/epoxy interface are systematically studied. A bilayer LDCB specimen is chosen to measure the interfacial fracture resistance. This specimen is calibrated by a model consisting of a beam on an elastic foundation which is validated by a finite-element analysis. The experimental results show that increasing surface roughness enhances the interfacial fracture resistance. Nonlinearity in this relation indicates that such an enhancement is caused not only by the increment of the actual contact area between the epoxy and the aluminum substrate due to roughness, but also by the change of local mode mixity, as well as bridging and friction behind the crack. The study shows that the important parameter governing the fracture resistance of aluminum/epoxy interface is the microscopic roughness index rather than the nanoscale pore size of the aluminum surface.

8 Acknowledgement

The work has been supported by U.S. Department of Energy Grant DEFG02-96ER45607. The authors would like to acknowledge the work carried out in the Center for Micro-analysis of Materials, FSMRL, University of Illinois, which is partially supported by the U.S. Department of Energy under grant DEFG02-91-ER45439. Helpful discussion

with Prof. A.G. Evans is acknowledged. The authors would like to thank Prof. A. Scheeline and Mr. H. Gao of the Chemistry Department at UIUC for providing Al samples with surfaces oxidized by the CRATER method. Thanks also go to Ming Liu of TAM Department at UIUC for his help during AFM scans in FSMRL.

References

1. H.M. Clearfield, D.K. McNamara and G.D. Davis, ASM Engineering Materials Handbook, Metals Park, OH, Vol. 3, pp. 259–275 (1990).

2. M.D. Thouless, Acta Metall. Mater. 40, 1281–1286 (1992).

3. M.D. Thouless, Scripta Metall. Mater. 26, 494–951(1992).

4. M.R. Turner, B.J. Dalgleish, M.Y. He and A.G. Evans, Acta Metall. Mater. 43 (9), 3459-3465 (1995).

5. M.R. Turner and A.G. Evans, Acta Mater. 44 (3), 863-871 (1996).

6. M. Y. He, A.G. Evans and J.W. Hutchinson, Acta Mater. 44 (7), 2963-2971 (1996).

7. M.D. Thouless, M.S. Kafkalidis, S.M. Ward and Y. Bankowski, Scripta Metall. 37, 1081–1087 (1997).

8. A. Cazzato and K.T. Faber, J. Am. Ceram. Soc 80 (1), 181-188 (1997).

9. A.J. Price and J.P. Sargent, Int. J. Adhesion and Adhesives 17, 27-32 (1997).

10. D.M. Brewis and G.W. Critchlow, Int. J. Adhesion and Adhesives 17, 33-38 (1997).

11. M. Kalnins, A. Sirmacs and L. Malers, Int. J. Adhesion and Adhesives 17, 365-372 (1997).

12. Y.L. Zhang and G.M. Spinks, J. Adhesion Sci. and Tech. 11, 207–223 (1997).

13. M.D. Thouless, J.L. Adams, M.S. Kafkalidis, S.M. Ward, R.A. Dickie and G.L. Westerbeek, J. Mater. Sci. 33, 187–197 (1998).

14. J.G. Swadener, L.M. Liechti and A.L. de Lozanne, J. Mech. Phys. Solids 47 (2), 223-258 (1999).

15. A. Mannelqvist and M.R. Groth, Appl. Phys. A 73, 347-355 (2001).

16. E. Sancaktar and R. Gomatam J. Adhesion Sci. and Technol. 15, 97-117 (2001).

17. S.L. Zhang, K.J. Hsia and A.J. Pearlstein, J. Mech. Phys. Solids 50 (3), 549-569 (2002).

18. S.L. Zhang and K.J. Hsia, ASME J. Appl. Mech. 68, 93-100 (2001).

19. T. Pardoen and J.W. Hutchinson, J. Mech. Phys. Solids 48 (12), 2467-2512 (2000).

20. Z. Suo and J.W. Hutchinson, Mat. Sci. Engng. A 107, 135-143 (1989).

21. H.C. Cao and A.G. Evans, Mech. Mater. 7, 295-305 (1989).

22. S. Yoshida, J. Matsuoka and N. Soga, J. Am. Ceram. Soc. 82 (6), 1621-1623 (1999).

23. S.N. Crichton, M. Tomozawa, J.S. Hayden, T.I. Suratwala and J.H. Campbell, J. Am. Ceram. Soc. 82 (11), 3097-3104 (1999).

24. A.G. Evans, J.W. Hutchinson and Y. Wei, Acta Mater. 47 (15), 4093-4113 (1999).

25. M.F. Kanninen, Int. J. Fract. 9 (1), 83-92 (1973).

26. G. Liu and J.K. Shang, Metall. Mater. Trans. A – Phys. Metall. and Mater. Sci. 27A, 213-219 (1996).

27. Z.H. Zhang and J.K. Shang, Metall. Mater. Trans. A – Phys. Metall. and Mater. Sci. 27A, 221-226 (1996).

28. H. Gao, A. Scheeline, and A.J. Pearlstein, Proceedings of the International Symposium on New Directions in Electroanalytical Chemistry, II, pp. 116-124, Electrochemcial Society, Pennington, NJ (1999).

29. H. Gao, A. Scheeline, and A.J. Pearlstein, J. Electrochem. Soc. 149 (6), B248-B255 (2002).

30. Y.-B. Xin, K.J. Hsia and D.A. Lange, J. Am. Ceram. Soc. 78 (12), 3201–3208 (1995).

31. X. Dai, M.V. Brillhart and P.S. Ho, IEEE Trans. on Components and Packaging Technology 23, 101–116 (2000).

32. J.W. Hutchinson and Z. Suo, Adv. Appl. Mech. 29, 64-189 (1992).

33. B.B. Mandelbrot, The Fractal Geometry of Nature. W.H. Freeman and Company, San Francisco (1982).

Table 1: Surface Treatment and Roughness Index

Specimen ID	Surface Treatments	Roughness Index (R)
SA-1	Sapphire surface	2.82E-07
O2-2	CRATER (2.8 V)	4.69E-05
O5-3	CRATER (5.8 V)	3.08E-05
O9-4	CRATER (9.6 V)	6.11E-05
DP-5	1 micron finish	3.89E-06
G600	600 grit finish	4.79E-03
G320	320 grit finish	2.90E-02
G180	180 grit finish	2.87E-02
G60	60 grit finish	5.84E-02

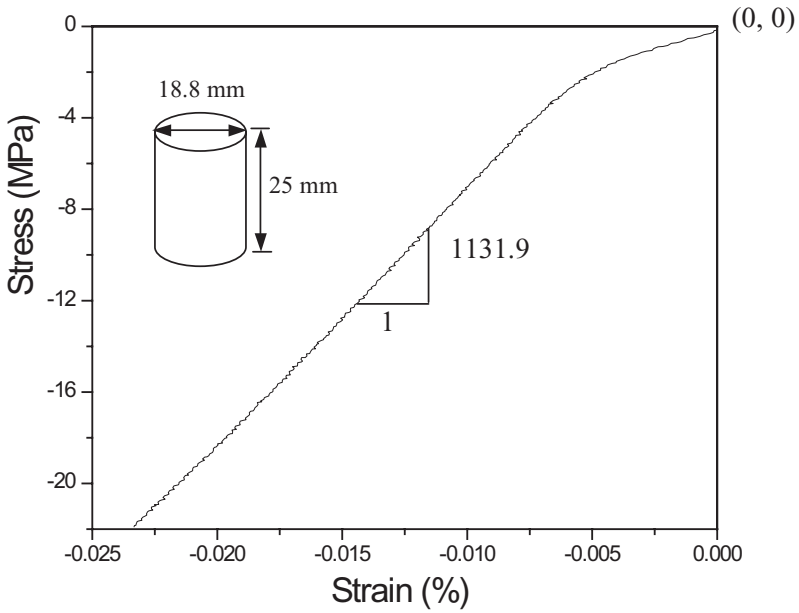

Figure 1: Stress–strain curve of the fully-cured epoxy (DP270).

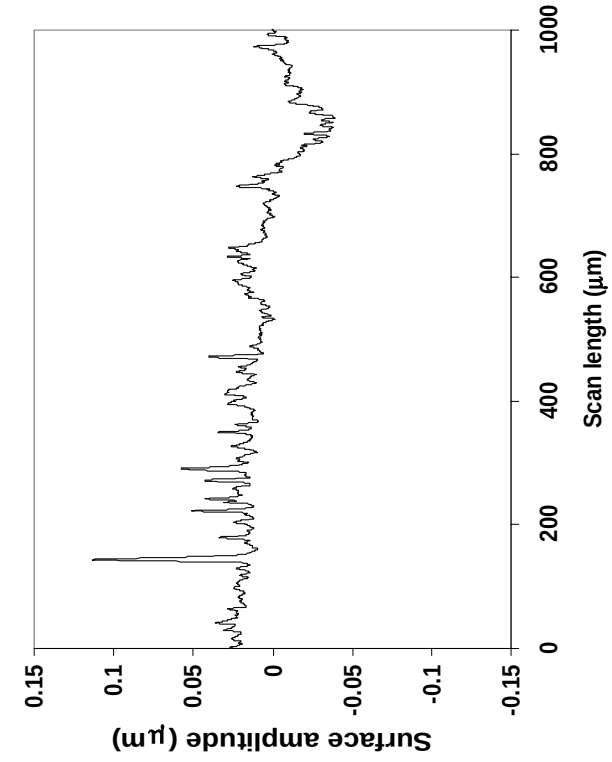

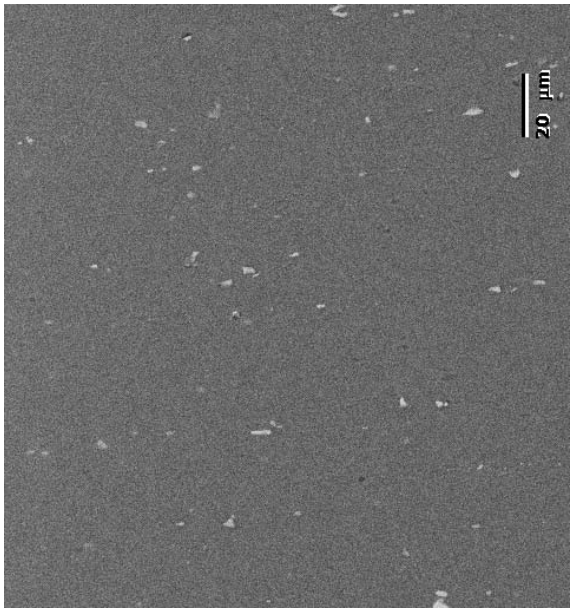

Figure 2: Aluminum surface polished by 1 micron diamond paste. (left) Scanning electron micrograph; (right) Line scan by profilometer.

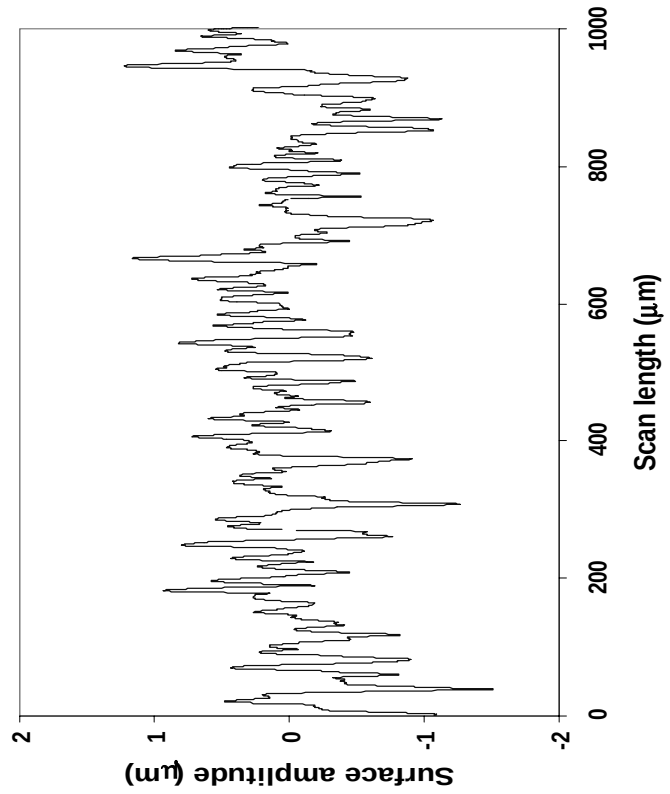

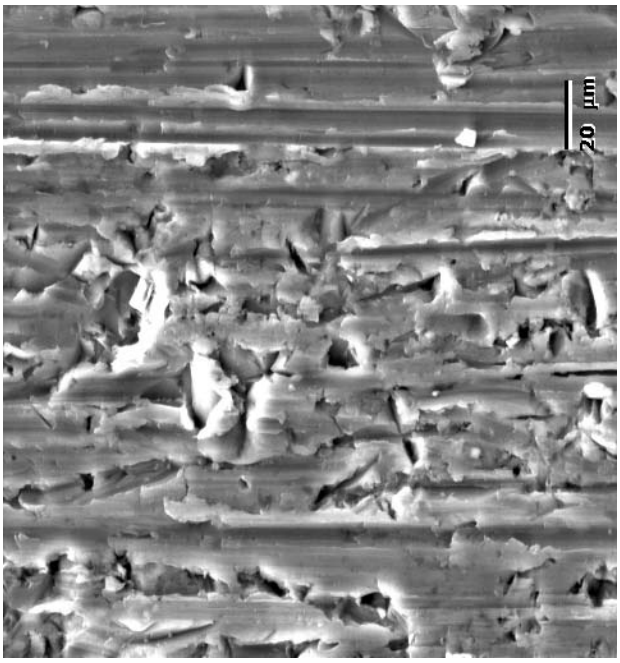

Figure 3: Aluminum surface polished by 600-grit SiC paper. (left) Scanning electron micrograph; (right) Line scan by profilometer.

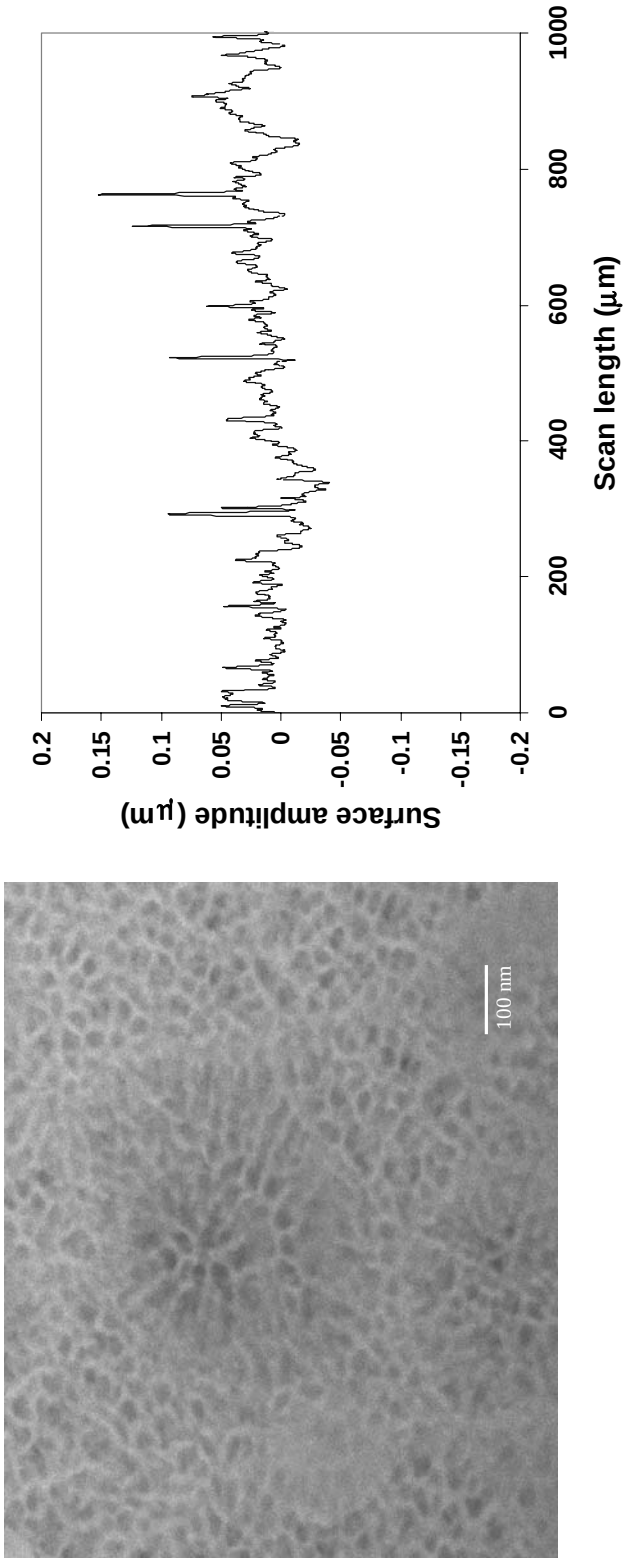

Figure 4: Aluminum surface oxidized by CRATER (applied potential: 9.6V). (left) Scanning electron micrograph; (right) Line scan by profilometer.

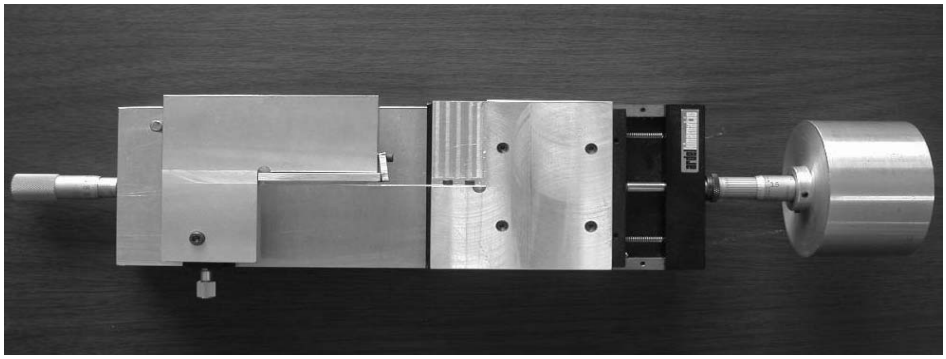

(a)

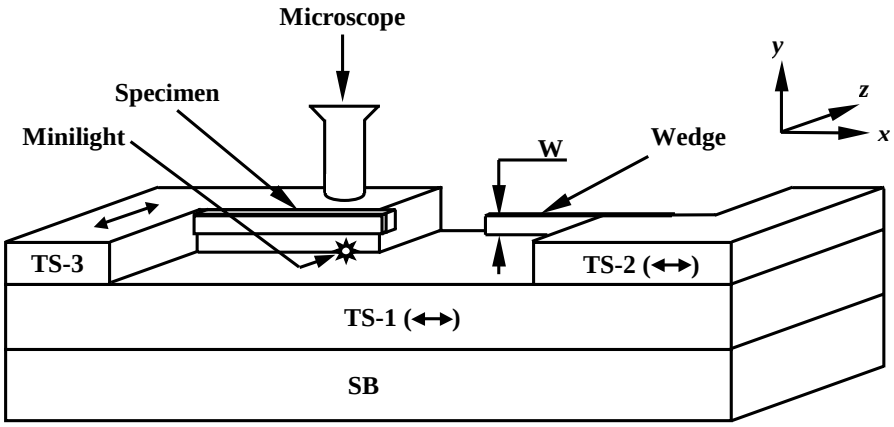

(b)

Figure 5: Testing apparatus (a) Image (top view); (b) Schematic.

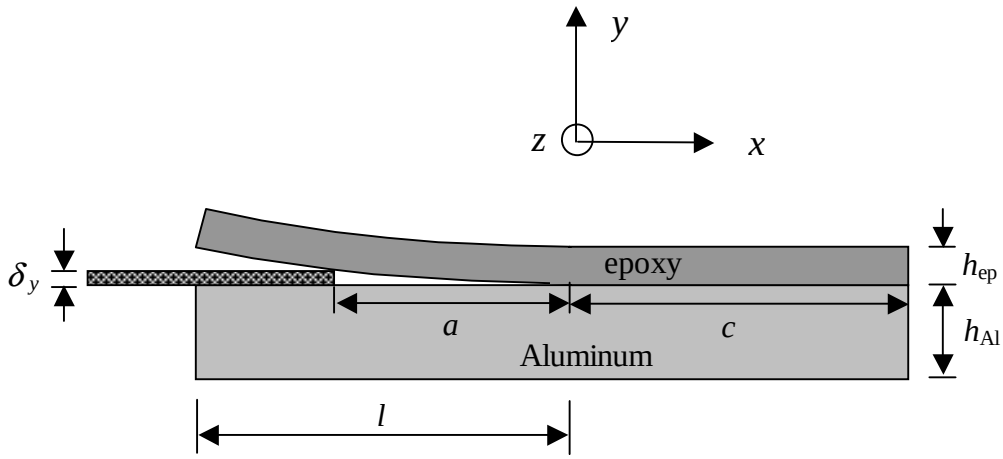

Figure 6: Schematic of the bilayer double cantilever beam (LDCB) specimen.

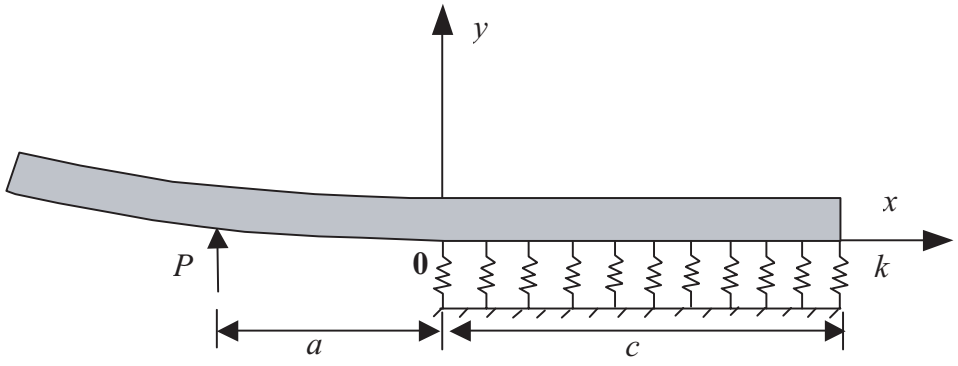

Figure 7: Beam on an elastic foundation model.

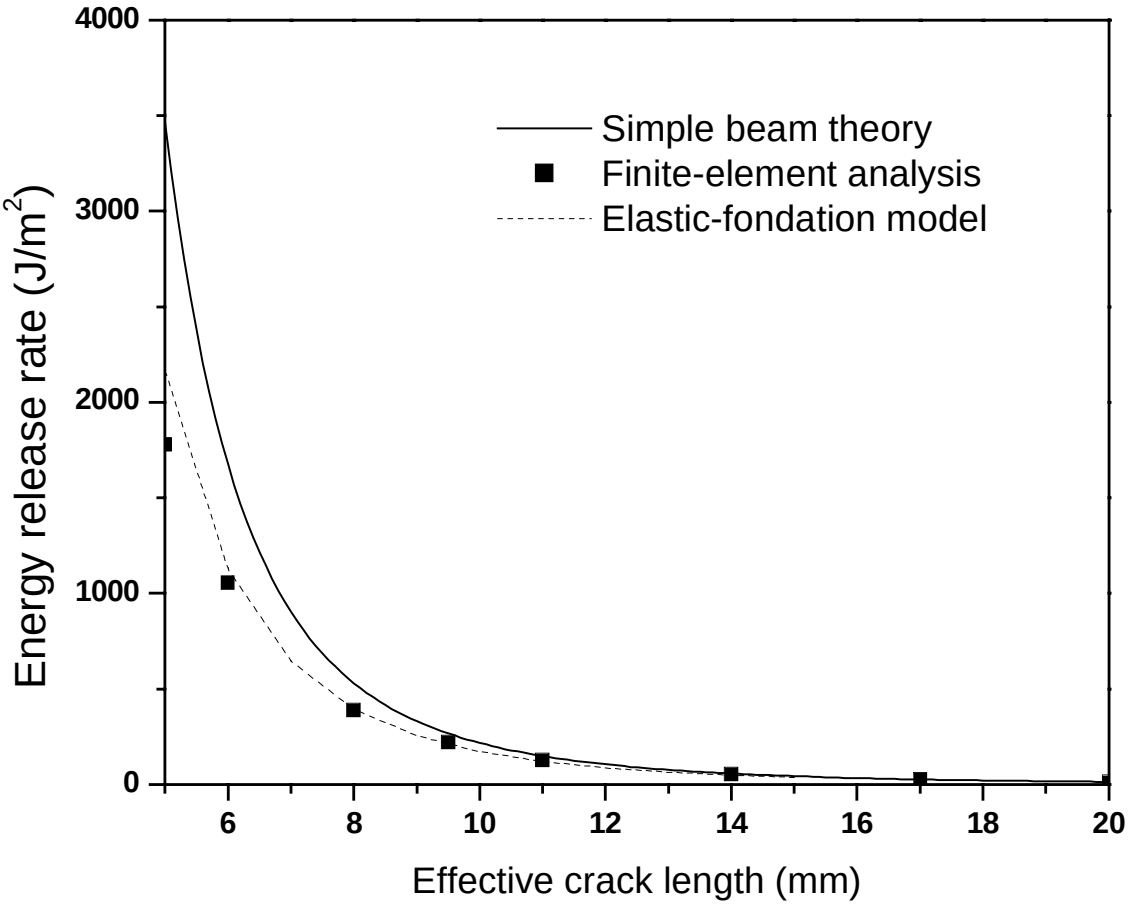

Figure 8: Calibration of the energy release rate.

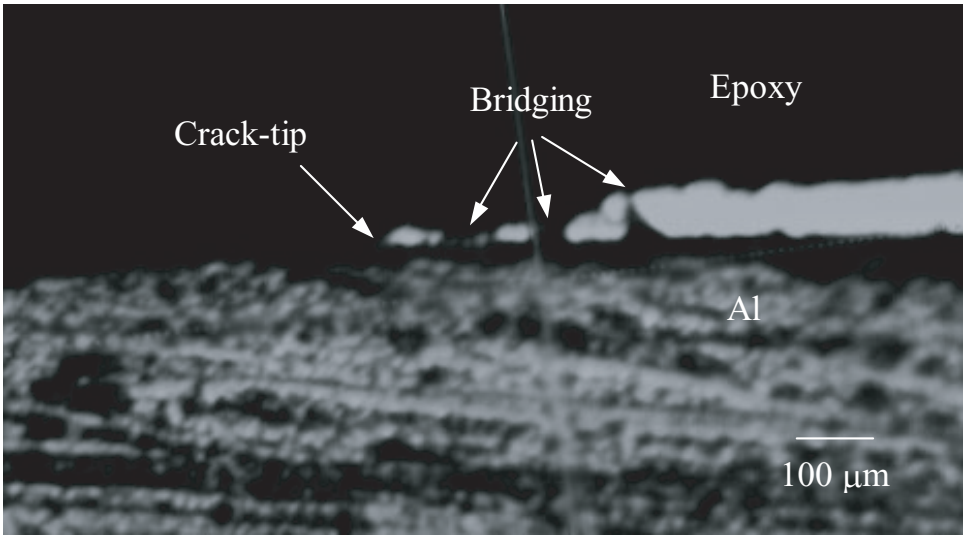

Figure 9: Bridging and surface fluctuations behind an extending interfacial crack (G60).

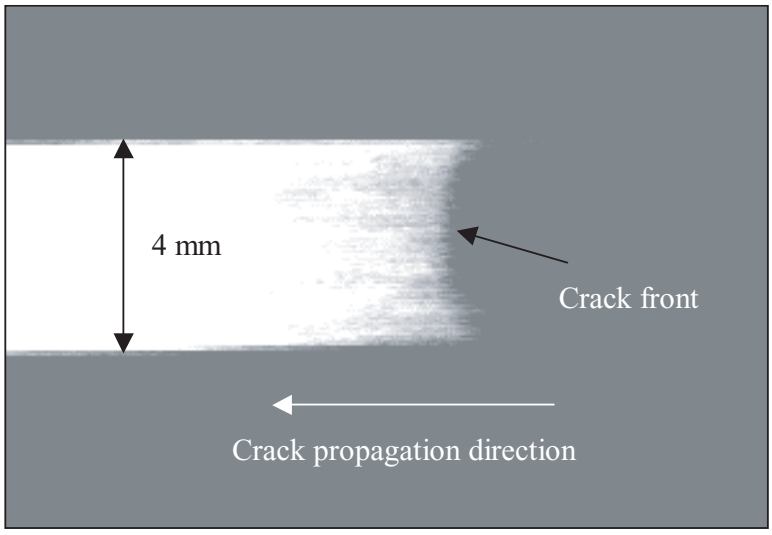

Figure 10: Crack front profile.

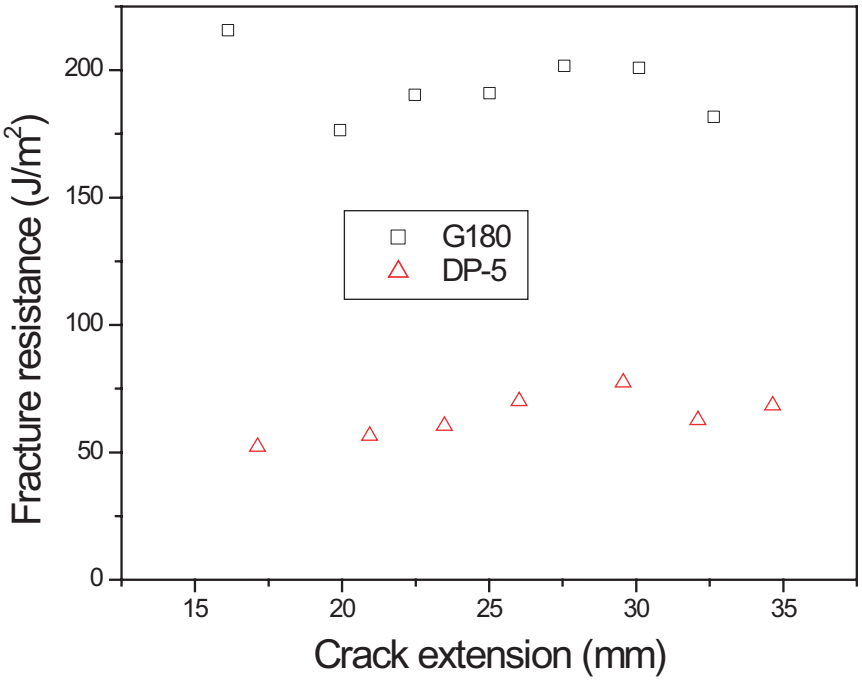

Figure 11: Fracture resistance versus the total debond length.

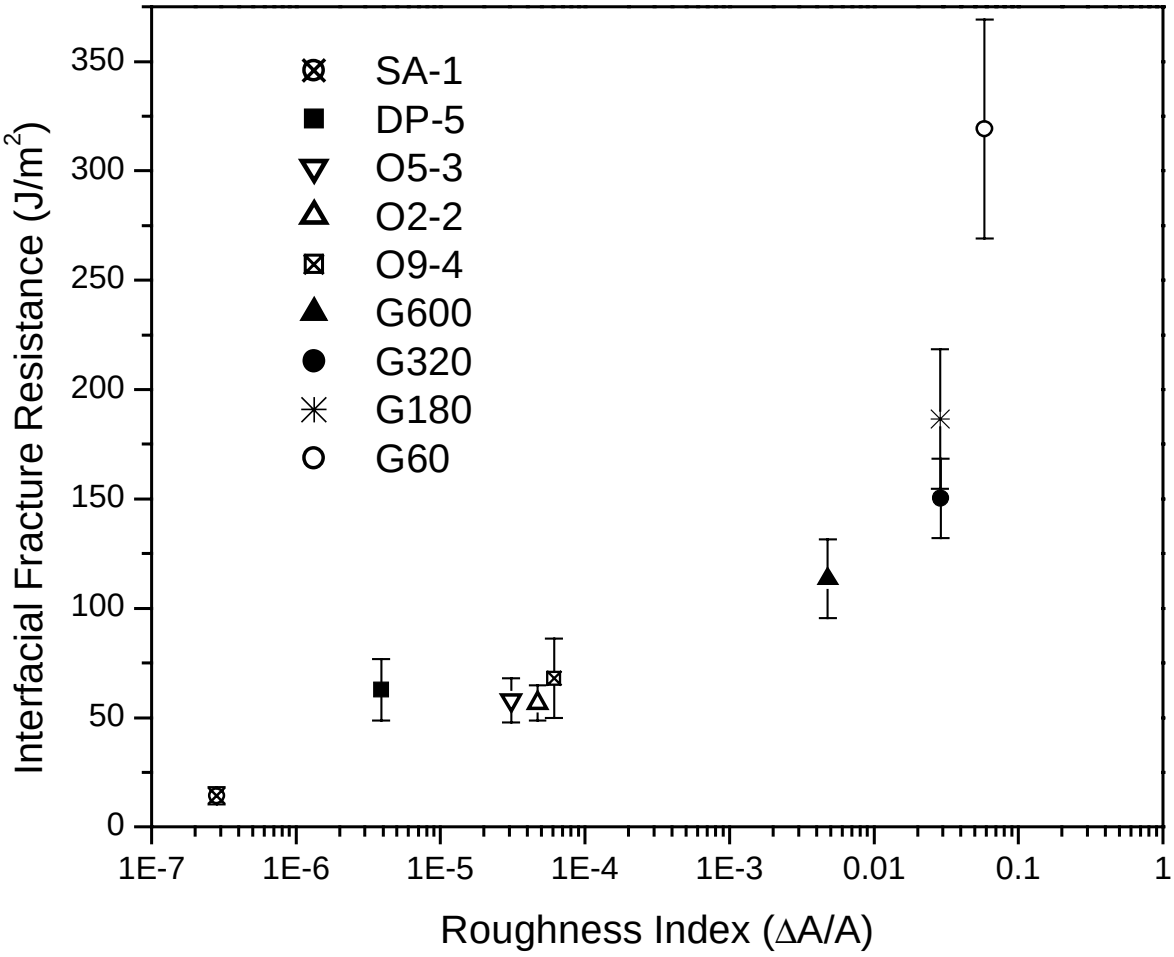

Figure 12: Interfacial fracture resistance as a function of aluminum surface roughness index.

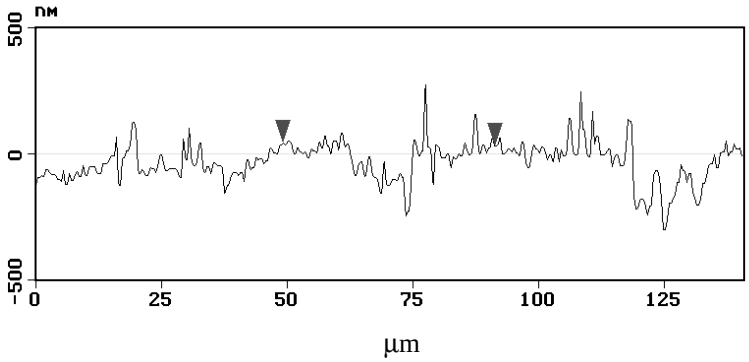

(a)

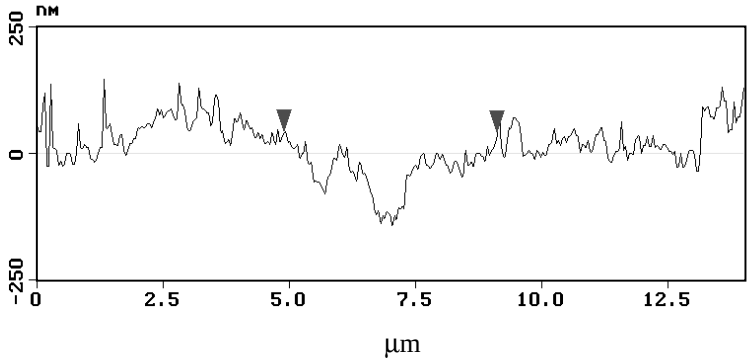

(b)

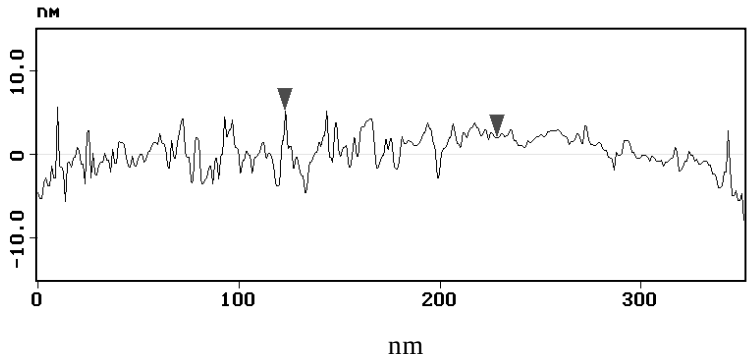

(c)

Figure 13: Topology of O9-4 using AFM scans at a lateral data resolution of (a) 400 nm, (b) 40 nm, and (c) 1 nm.

List of Recent TAM Reports

No.	*Authors*	*Title*	*Date*
927	Ferry, J. P., and S. Balachandar	A fast Eulerian method for two-phase flow—*International Journal of Multiphase Flow*, in press (2000)	Feb. 2000
928	Thoroddsen, S. T., and K. Takehara	The coalescence–cascade of a drop—*Physics of Fluids* **12**, 1257–1265 (2000)	Feb. 2000
929	Liu, Z.-C., R. J. Adrian, and T. J. Hanratty	Large-scale modes of turbulent channel flow: Transport and structure—*Journal of Fluid Mechanics* **448**, 53–80 (2001)	Feb. 2000
930	Borodai, S. G., and R. D. Moser	The numerical decomposition of turbulent fluctuations in a compressible boundary layer—*Theoretical and Computational Fluid Dynamics* (submitted)	Mar. 2000
931	Balachandar, S., and F. M. Najjar	Optimal two-dimensional models for wake flows—*Physics of Fluids*, in press (2000)	Mar. 2000
932	Yoon, H. S., K. V. Sharp, D. F. Hill, R. J. Adrian, S. Balachandar, M. Y. Ha, and K. Kar	Integrated experimental and computational approach to simulation of flow in a stirred tank—*Chemical Engineering Sciences* **56**, 6635–6649 (2001)	Mar. 2000
933	Sakakibara, J., Hishida, K., and W. R. C. Phillips	On the vortical structure in a plane impinging jet—*Journal of Fluid Mechanics* **434**, 273–300 (2001)	Apr. 2000
934	Phillips, W. R. C.	Eulerian space–time correlations in turbulent shear flows—*Physics of Fluids* **12**, 2056–2064 (2000)	Apr. 2000
935	Hsui, A. T., and D. N. Riahi	Onset of thermal–chemical convection with crystallization within a binary fluid and its geological implications—*Geochemistry, Geophysics, Geosystems* **2**, 2000GC000075 (2001)	Apr. 2000
936	Cermelli, P., E. Fried, and S. Sellers	Configurational stress, yield, and flow in rate-independent plasticity—*Proceedings of the Royal Society of London A* **457**, 1447–1467 (2001)	Apr. 2000
937	Adrian, R. J., C. Meneveau, R. D. Moser, and J. J. Riley	Final report on 'Turbulence Measurements for Large-Eddy Simulation' workshop	Apr. 2000
938	Bagchi, P., and S. Balachandar	Linearly varying ambient flow past a sphere at finite Reynolds number—Part 1: Wake structure and forces in steady straining flow	Apr. 2000
939	Gioia, G., A. DeSimone, M. Ortiz, and A. M. Cuitiño	Folding energetics in thin-film diaphragms—*Proceedings of the Royal Society of London A* **458**, 1223–1229 (2002)	Apr. 2000
940	Chaïeb, S., and G. H. McKinley	Mixing immiscible fluids: Drainage induced cusp formation	May 2000
941	Thoroddsen, S. T., and A. Q. Shen	Granular jets—*Physics of Fluids* **13**, 4–6 (2001)	May 2000
942	Riahi, D. N.	Non-axisymmetric chimney convection in a mushy layer under a high-gravity environment—In *Centrifugal Materials Processing* (L. L. Regel and W. R. Wilcox, eds.), 295–302 (2001)	May 2000
943	Christensen, K. T., S. M. Soloff, and R. J. Adrian	PIV Sleuth: Integrated particle image velocimetry interrogation/validation software	May 2000
944	Wang, J., N. R. Sottos, and R. L. Weaver	Laser induced thin film spallation—*Experimental Mechanics* (submitted)	May 2000
945	Riahi, D. N.	Magnetohydrodynamic effects in high gravity convection during alloy solidification—In *Centrifugal Materials Processing* (L. L. Regel and W. R. Wilcox, eds.), 317–324 (2001)	June 2000
946	Gioia, G., Y. Wang, and A. M. Cuitiño	The energetics of heterogeneous deformation in open-cell solid foams—*Proceedings of the Royal Society of London A* **457**, 1079–1096 (2001)	June 2000

List of Recent TAM Reports (cont'd)

No.	Authors	Title	Date
947	Kessler, M. R., and S. R. White	Self-activated healing of delamination damage in woven composites—*Composites A: Applied Science and Manufacturing* **32**, 683–699 (2001)	June 2000
948	Phillips, W. R. C.	On the pseudomomentum and generalized Stokes drift in a spectrum of rotational waves—*Journal of Fluid Mechanics* **430**, 209–229 (2001)	July 2000
949	Hsui, A. T., and D. N. Riahi	Does the Earth's nonuniform gravitational field affect its mantle convection?—*Physics of the Earth and Planetary Interiors* (submitted)	July 2000
950	Phillips, J. W.	Abstract Book, 20th International Congress of Theoretical and Applied Mechanics (27 August – 2 September, 2000, Chicago)	July 2000
951	Vainchtein, D. L., and H. Aref	Morphological transition in compressible foam—*Physics of Fluids* **13**, 2152–2160 (2001)	July 2000
952	Chaïeb, S., E. Sato-Matsuo, and T. Tanaka	Shrinking-induced instabilities in gels	July 2000
953	Riahi, D. N., and A. T. Hsui	A theoretical investigation of high Rayleigh number convection in a nonuniform gravitational field—*Acta Mechanica* (submitted)	Aug. 2000
954	Riahi, D. N.	Effects of centrifugal and Coriolis forces on a hydromagnetic chimney convection in a mushy layer—*Journal of Crystal Growth* **226**, 393–405 (2001)	Aug. 2000
955	Fried, E.	An elementary molecular-statistical basis for the Mooney and Rivlin–Saunders theories of rubber-elasticity—*Journal of the Mechanics and Physics of Solids* **50**, 571–582 (2002)	Sept. 2000
956	Phillips, W. R. C.	On an instability to Langmuir circulations and the role of Prandtl and Richardson numbers—*Journal of Fluid Mechanics* **442**, 335–358 (2001)	Sept. 2000
957	Chaïeb, S., and J. Sutin	Growth of myelin figures made of water soluble surfactant—Proceedings of the 1st Annual International IEEE–EMBS Conference on Microtechnologies in Medicine and Biology (October 2000, Lyon, France), 345–348	Oct. 2000
958	Christensen, K. T., and R. J. Adrian	Statistical evidence of hairpin vortex packets in wall turbulence—*Journal of Fluid Mechanics* **431**, 433–443 (2001)	Oct. 2000
959	Kuznetsov, I. R., and D. S. Stewart	Modeling the thermal expansion boundary layer during the combustion of energetic materials—*Combustion and Flame*, in press (2001)	Oct. 2000
960	Zhang, S., K. J. Hsia, and A. J. Pearlstein	Potential flow model of cavitation-induced interfacial fracture in a confined ductile layer—*Journal of the Mechanics and Physics of Solids*, **50**, 549–569 (2002)	Nov. 2000
961	Sharp, K. V., R. J. Adrian, J. G. Santiago, and J. I. Molho	Liquid flows in microchannels—Chapter 6 of *CRC Handbook of MEMS* (M. Gad-el-Hak, ed.) (2001)	Nov. 2000
962	Harris, J. G.	Rayleigh wave propagation in curved waveguides—*Wave Motion* **36**, 425–441 (2002)	Jan. 2001
963	Dong, F., A. T. Hsui, and D. N. Riahi	A stability analysis and some numerical computations for thermal convection with a variable buoyancy factor—*Journal of Theoretical and Applied Mechanics*, in press (2002)	Jan. 2001
964	Phillips, W. R. C.	Langmuir circulations beneath growing or decaying surface waves—*Journal of Fluid Mechanics* (submitted)	Jan. 2001
965	Bdzil, J. B., D. S. Stewart, and T. L. Jackson	Program burn algorithms based on detonation shock dynamics—*Journal of Computational Physics* (submitted)	Jan. 2001
966	Bagchi, P., and S. Balachandar	Linearly varying ambient flow past a sphere at finite Reynolds number: Part 2—Equation of motion—*Journal of Fluid Mechanics* (submitted)	Feb. 2001
967	Cermelli, P., and E. Fried	The evolution equation for a disclination in a nematic fluid—*Proceedings of the Royal Society A* **458**, 1–20 (2002)	Apr. 2001

List of Recent TAM Reports (cont'd)

No.	Authors	Title	Date
968	Riahi, D. N.	Effects of rotation on convection in a porous layer during alloy solidification—Chapter 12 in *Transport Phenomena in Porous Media* (D. B. Ingham and I. Pop, eds.), 316–340 (2002)	Apr. 2001
969	Damljanovic, V., and R. L. Weaver	Elastic waves in cylindrical waveguides of arbitrary cross section—*Journal of Sound and Vibration* (submitted)	May 2001
970	Gioia, G., and A. M. Cuitiño	Two-phase densification of cohesive granular aggregates—*Physical Review Letters* **88**, 204302 (2002) (in extended form and with added co-authors S. Zheng and T. Uribe)	May 2001
971	Subramanian, S. J., and P. Sofronis	Calculation of a constitutive potential for isostatic powder compaction—*International Journal of Mechanical Sciences* (submitted)	June 2001
972	Sofronis, P., and I. M. Robertson	Atomistic scale experimental observations and micromechanical/ continuum models for the effect of hydrogen on the mechanical behavior of metals—*Philosophical Magazine* (submitted)	June 2001
973	Pushkin, D. O., and H. Aref	Self-similarity theory of stationary coagulation—*Physics of Fluids* **14**, 694–703 (2002)	July 2001
974	Lian, L., and N. R. Sottos	Stress effects in ferroelectric thin films—*Journal of the Mechanics and Physics of Solids* (submitted)	Aug. 2001
975	Fried, E., and R. E. Todres	Prediction of disclinations in nematic elastomers—*Proceedings of the National Academy of Sciences* **98**, 14773–14777 (2001)	Aug. 2001
976	Fried, E., and V. A. Korchagin	Striping of nematic elastomers—*International Journal of Solids and Structures* **39**, 3451–3467 (2002)	Aug. 2001
977	Riahi, D. N.	On nonlinear convection in mushy layers: Part I. Oscillatory modes of convection—*Journal of Fluid Mechanics* **467**, 331–359 (2002)	Sept. 2001
978	Sofronis, P., I. M. Robertson, Y. Liang, D. F. Teter, and N. Aravas	Recent advances in the study of hydrogen embrittlement at the University of Illinois—Invited paper, Hydrogen–Corrosion Deformation Interactions (Sept. 16–21, 2001, Jackson Lake Lodge, Wyo.)	Sept. 2001
979	Fried, E., M. E. Gurtin, and K. Hutter	A void-based description of compaction and segregation in flowing granular materials—*Proceedings of the Royal Society of London A* (submitted)	Sept. 2001
980	Adrian, R. J., S. Balachandar, and Z.-C. Liu	Spanwise growth of vortex structure in wall turbulence—*Korean Society of Mechanical Engineers International Journal* **15**, 1741–1749 (2001)	Sept. 2001
981	Adrian, R. J.	Information and the study of turbulence and complex flow—*Japanese Society of Mechanical Engineers Journal B*, in press (2002)	Oct. 2001
982	Adrian, R. J., and Z.-C. Liu	Observation of vortex packets in direct numerical simulation of fully turbulent channel flow—*Journal of Visualization*, in press (2002)	Oct. 2001
983	Fried, E., and R. E. Todres	Disclinated states in nematic elastomers—*Journal of the Mechanics and Physics of Solids* **50**, 2691–2716 (2002)	Oct. 2001
984	Stewart, D. S.	Towards the miniaturization of explosive technology—Proceedings of the 23rd International Conference on Shock Waves (2001)	Oct. 2001
985	Kasimov, A. R., and Stewart, D. S.	Spinning instability of gaseous detonations—*Journal of Fluid Mechanics* (submitted)	Oct. 2001
986	Brown, E. N., N. R. Sottos, and S. R. White	Fracture testing of a self-healing polymer composite—*Experimental Mechanics* (submitted)	Nov. 2001
987	Phillips, W. R. C.	Langmuir circulations—*Surface Waves* (J. C. R. Hunt and S. Sajjadi, eds.), in press (2002)	Nov. 2001
988	Gioia, G., and F. A. Bombardelli	Scaling and similarity in rough channel flows—*Physical Review Letters* **88**, 014501 (2002)	Nov. 2001
989	Riahi, D. N.	On stationary and oscillatory modes of flow instabilities in a rotating porous layer during alloy solidification—*Journal of Porous Media*, in press (2002)	Nov. 2001
990	Okhuysen, B. S., and D. N. Riahi	Effect of Coriolis force on instabilities of liquid and mushy regions during alloy solidification—*Physics of Fluids* (submitted)	Dec. 2001

List of Recent TAM Reports (cont'd)

No.	*Authors*	*Title*	*Date*
991	Christensen, K. T., and R. J. Adrian	Measurement of instantaneous Eulerian acceleration fields by particle-image accelerometry: Method and accuracy—*Experimental Fluids* (submitted)	Dec. 2001
992	Liu, M., and K. J. Hsia	Interfacial cracks between piezoelectric and elastic materials under in-plane electric loading—*Journal of the Mechanics and Physics of Solids* (submitted)	Dec. 2001
993	Panat, R. P., S. Zhang, and K. J. Hsia	Bond coat surface rumpling in thermal barrier coatings—*Acta Materialia*, in press (2002)	Jan. 2002
994	Aref, H.	A transformation of the point vortex equations—*Physics of Fluids* **14**, 2395–2401 (2002)	Jan. 2002
995	Saif, M. T. A, S. Zhang, A. Haque, and K. J. Hsia	Effect of native Al_2O_3 on the elastic response of nanoscale aluminum films—*Acta Materialia* **50**, 2779–2786 (2002)	Jan. 2002
996	Fried, E., and M. E. Gurtin	A nonequilibrium theory of epitaxial growth that accounts for surface stress and surface diffusion—*Journal of the Mechanics and Physics of Solids*, in press (2002)	Jan. 2002
997	Aref, H.	The development of chaotic advection—*Physics of Fluids* **14**, 1315–1325 (2002); see also *Virtual Journal of Nanoscale Science and Technology*, 11 March 2002	Jan. 2002
998	Christensen, K. T., and R. J. Adrian	The velocity and acceleration signatures of small-scale vortices in turbulent channel flow—*Journal of Turbulence*, in press (2002)	Jan. 2002
999	Riahi, D. N.	Flow instabilities in a horizontal dendrite layer rotating about an inclined axis—*Proceedings of the Royal Society of London A* (submitted)	Feb. 2002
1000	Kessler, M. R., and S. R. White	Cure kinetics of ring-opening metathesis polymerization of dicyclopentadiene—*Journal of Polymer Science A* **40**, 2373–2383 (2002)	Feb. 2002
1001	Dolbow, J. E., E. Fried, and A. Q. Shen	Point defects in nematic gels: The case for hedgehogs—*Proceedings of the National Academy of Sciences* (submitted)	Feb. 2002
1002	Riahi, D. N.	Nonlinear steady convection in rotating mushy layers—*Journal of Fluid Mechanics* (submitted)	Mar. 2002
1003	Carlson, D. E., E. Fried, and S. Sellers	The totality of soft-states in a neo-classical nematic elastomer—*Proceedings of the Royal Society A* (submitted)	Mar. 2002
1004	Fried, E., and R. E. Todres	Normal-stress differences and the detection of disclinations in nematic elastomers—*Journal of Polymer Science B: Polymer Physics*, in **40**, 2098–2106 (2002)	June 2002
1005	Fried, E., and B. C. Roy	Gravity-induced segregation of cohesionless granular mixtures—*Lecture Notes in Mechanics*, in press (2002)	July 2002
1006	Tomkins, C. D., and R. J. Adrian	Spanwise structure and scale growth in turbulent boundary layers—*Journal of Fluid Mechanics* (submitted)	Aug. 2002
1007	Riahi, D. N.	On nonlinear convection in mushy layers: Part 2. Mixed oscillatory and stationary modes of convection—*Journal of Fluid Mechanics* (submitted)	Sept. 2002
1008	Aref, H., P. K. Newton, M. A. Stremler, T. Tokieda, and D. L. Vainchtein	Vortex crystals—*Advances in Applied Mathematics* **39**, in press (2002)	Oct. 2002
1009	Bagchi, P., and S. Balachandar	Effect of turbulence on the drag and lift of a particle—*Physics of Fluids* (submitted)	Oct. 2002
1010	Zhang, S., R. Panat, and K. J. Hsia	Influence of surface morphology on the adhesive strength of aluminum/epoxy interfaces—*Journal of Adhesion Science and Technology* (submitted)	Oct. 2002